Sensitivity of Gas-Evolving Electrocatalysis to the Catalyst Microenvironment

Kaige Shi,[1] Zackary S. Parsons,[1] and Xiaofeng Feng[1,2,3,4]*

[1]Department of Physics, University of Central Florida, Orlando, Florida 32816, United States

[2]Renewable Energy and Chemical Transformations (REACT) Cluster, University of Central Florida, Orlando, Florida 32816, United States

[3]Department of Chemistry, University of Central Florida, Orlando, Florida 32816, United States

[4]Department of Materials Science and Engineering, University of Central Florida, Orlando, Florida 32816, United States

*Email: Xiaofeng.Feng@ucf.edu (X.F.)

ABSTRACT:

Many electrochemical reactions for the development of renewable energy technologies are gas-evolving reactions, where the electrocatalytic performance is susceptible to the wetting properties of catalyst microenvironment. Here, using N_2H_4 electro-oxidation to N_2 on carbon-supported Pt nanocatalysts as a model reaction, we controlled the microenvironment using oxygen-doped and fluorine-doped carbon supports to make it more hydrophilic and more hydrophobic, respectively, and elucidated the effect on the reaction kinetics. The electrode with oxygen-doped carbon showed a 123% higher activity than that with pristine carbon, benefiting from the increased wetting and exposure of Pt catalytic sites to the electrolyte. Counterintuitively, the electrode with fluorine-doped carbon also exhibited a 46% higher activity than that with pristine carbon, despite its lower wetting of Pt. We found that the hydrophobic microenvironment accelerated the surface diffusion, coalescence, and detachment of the generated N_2 gas bubbles, which would otherwise block the Pt active sites from catalyzing the reaction.

Electrocatalysis plays a central role in the development of renewable energy technologies including fuel cells and electrolyzers, as it can facilitate direct and efficient conversion between renewable electricity and chemical energy.[1] On one hand, fuel cells can convert the chemical energy in fuels to generate electricity, such as hydrogen fuel cells.[2] On the other hand, electrolyzers are being developed for renewably powered electrosynthesis of chemicals and fuels, such as water splitting to generate hydrogen and CO_2 reduction to produce hydrocarbons and oxygenates.[3,4] The major challenge for developing such technologies still lies in the rational design of active, selective, and durable electrocatalysts.[5] However, in addition to solid catalysts, the electrocatalytic processes typically involve liquid electrolyte (including molecules and ions dissolved in the electrolyte) and gaseous species, bringing an intrinsic complexity to the local environment around catalytic sites, which may have a significant impact on the distribution and mass transport of reaction species and thus affect the electrocatalytic performance.[6−10]

For gas-involving electrocatalytic reactions, an important property of the microenvironment is the wetting characteristics, as a hydrophilic surface (contact angle < 90°) favors liquid while a hydrophobic surface (contact angle > 90°) favors gas.[11] The hydrophilicity/hydrophobicity of a microenvironment determines the distribution and diffusion of liquid and gaseous species around catalysts, thus impacting the reaction kinetics. For example, for the electroreduction of CO_2, the reaction rate is often limited by the mass transport of CO_2 at high overpotentials due to the slow diffusion of CO_2 dissolved in aqueous electrolyte.[12] The CO_2 electrolysis can be improved by creating a hydrophobic microenvironment, which can trap CO_2 gas bubbles near the catalysts and accelerate CO_2 mass transport.[6,8] Therefore, for reactions with a gaseous reactant, a moderately hydrophobic microenvironment may be beneficial because it can establish and maintain a balance between liquid electrolyte and gaseous reactant in the catalyst layer, so that the interaction between the three phases (solid catalyst, liquid electrolyte, and gaseous reactant) can be further optimized for efficient electrocatalysis.[10,13]

In gas evolution reactions such as hydrogen evolution reaction (HER) and hydrazine (N_2H_4) oxidation to N_2, the formation and detachment of gas bubbles impact the exposure of catalytic sites to liquid electrolyte,[14−19] and thus affect the reaction kinetics and mass and energy transfer.[20,21] The dynamics of gas bubbles depend on the adhesion force between the bubbles and the electrode surface, which further depends on the wetting properties and morphology of the electrodes.[22−24] Accordingly, many efforts have been made to improve gas-evolving electrocatalysis by designing electrodes with optimized gas bubble release. A typical strategy is to prepare superaerophobic or superhydrophilic electrodes with nanostructured morphology (such as nanowire- or nanotube-array electrodes),[25−32] which can decrease the adhesion force of gas bubbles and thus release the in situ generated gas bubbles in a timely manner and at smaller sizes.

Here, we investigate the effect of the microenvironment, particularly the wetting properties, on gas-evolving electrocatalysis, using the electro-oxidation of N_2H_4 to N_2 gas on Pt catalyst as a model system. In contrast to previous studies focused on the nanomorphology of electrodes, we look into the carbon black that has been widely used as the catalyst support in electrocatalysis,[33−36] and use heteroatom doping to tune the carbon support over a wide range of wetting conditions: O-doping makes it more hydrophilic while F-doping increases the hydrophobicity. We find that both O-doped and F-doped electrodes show enhanced electrocatalytic performances, which are however attributed to different factors in the electrocatalytic process: the O-doped carbon increases the wetting and exposure of Pt catalytic sites to aqueous N_2H_4, while the F-doped carbon accelerates the diffusion and detachment of the in situ generated N_2 gas bubbles. Therefore, we demonstrate that gas-evolving electrocatalysis is highly sensitive to the catalyst microenvironment, which thus should be considered and utilized in the design of efficient electrocatalysts and electrodes.

In electrocatalysis, carbon nanomaterials have often been employed as a support to disperse the catalyst nanoparticles,[33−35] which thus allows the tuning of the catalyst microenvironment via the carbon support. Here we start with the widely used Vulcan XC-72 carbon black and change its wetting properties by heteroatom doping,[36] thus enabling the investigation and comparison of the catalyst microenvironment. We first prepared O-doped carbon black by acidification treatment of the pristine carbon black in nitric acid for 12 h (see the Experimental Methods in the Supporting Information for details),[37] and the derived carbon sample is referred to as C-O-12. The acidification treatment introduced C−O and C=O functional groups,[37] which can enhance the surface interaction with water and the hydrophilicity of the carbon black. For comparison, we also prepared F-doped carbon black by pyrolysis of PTFE nanopowder mixed with Vulcan XC-72 carbon black at 950 °C under Ar/H_2 gas flow (see the Experimental Methods in the Supporting Information for details). A representative F-doped carbon sample was derived from an initial mixture of 100 mg carbon black and 800 mg PTFE, which is hereafter referred to as C-F-800. The F-doping makes the carbon black more hydrophobic due to the "polar hydrophobicity" of fluorinated carbon groups that have a negligible electrostatic interaction with water.[38]

The pristine and doped carbon black samples were characterized using transmission electron microscopy (TEM) and X-ray photoelectron spectroscopy (XPS) to examine their morphology and composition. As shown in Figure 1a−c, the TEM images suggest that the pristine, O-doped, and F-doped carbon samples all consist of amorphous carbon nanoparticles with a similar morphology. Statistical size distributions derived from the TEM images indicate that the average particle sizes in the three samples are 34.8 ± 10.6 nm, 34.1 ± 12.0 nm, and 32.4 ± 11.3 nm, respectively. Thus, the doping treatment had no apparent influence on the particle size and morphology of the carbon black. The XPS survey spectra of the three samples are presented in Figure 1d, with high-resolution XPS spectra of O 1s and F 1s peaks shown in Figure 1e and 1f, respectively. Only carbon and a small amount of oxygen are identified in the pristine carbon black, of which the latter is attributed

to native oxide. The intensity of the O 1s peak at ~532 eV increases substantially in the O-doped sample, confirming the introduction of oxygen dopants in the form of oxygen functional groups.[37] The F-doped carbon black shows an O 1s peak of similar intensity to that in the pristine carbon black, while the F 1s peak emerges at ~686 eV, confirming the presence of fluorine dopants in the sample. Energy dispersive spectroscopy (EDS) was used to roughly estimate the concentration of dopants. The atomic percentage of oxygen in the pristine carbon black is found to be 4.1%, which increases to 13.1% in the C-O-12 sample. While the pristine carbon black does not contain fluorine, the atom percentage of fluorine in the C-F-800 sample is around 3.1%.[10]

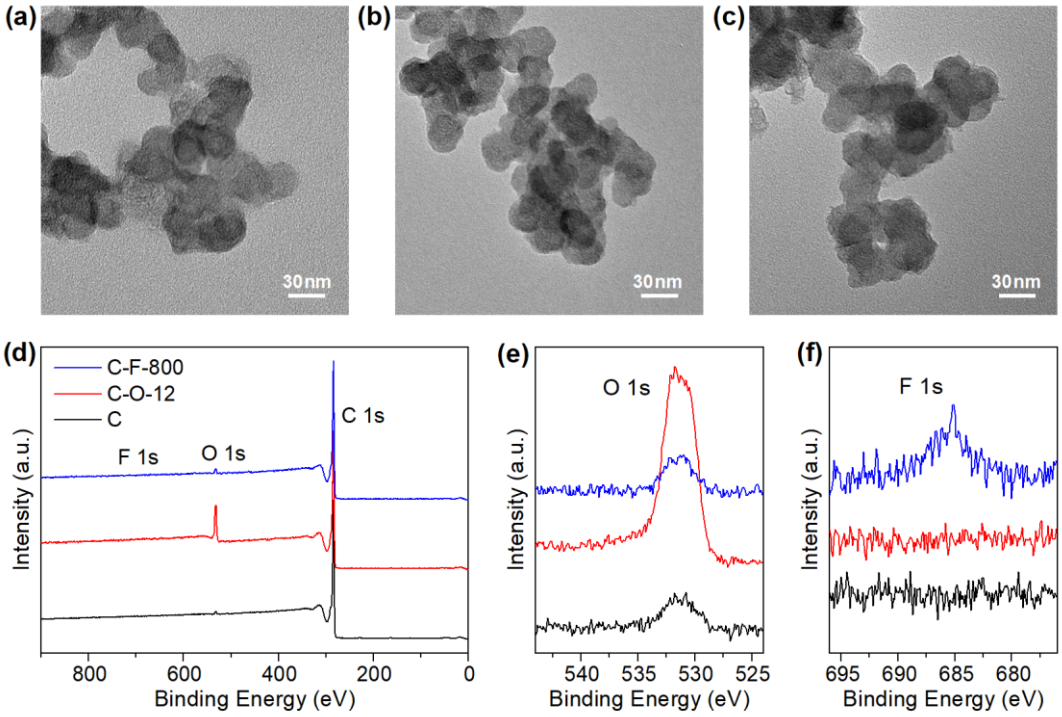

Figure 1. Characterization of the carbon black samples. (a–c) Representative TEM images of the (a) pristine carbon black, (b) C-O-12, and (c) C-F-800 samples. (d–f) XPS survey spectra (d) and high-resolution XPS spectra of O 1s (e) and F 1s (f) peaks for the three carbon samples.

The carbon black samples (pristine, O-doped, or F-doped) were each mixed with commercial Pt/C nanoparticles (20% Pt on Vulcan XC-72) and Nafion solution (5 wt%) to form a uniform catalyst ink, which was drop-casted onto a piece of carbon substrate to form an electrode (see the Experimental Methods in the Supporting Information for details). The Pt nanoparticles were also characterized by TEM and X-ray diffraction (XRD) to examine their size and structure. As shown in Figure S1, typical TEM image and corresponding particle size distribution reveal an average size of 3.0 ± 0.7 nm of the Pt nanoparticles. As expected, the XRD pattern in Figure S1c exhibit four diffraction peaks that correspond to carbon, Pt(111), Pt(200), and Pt(220) planes, respectively.

Thus, three electrodes were prepared with the same Pt nanocatalyst but different carbon supports, which are hereafter referred to as the Pt/C, Pt/C-O-12, and Pt/C-F-800 electrodes, respectively. As shown in Figure 2a–c, the scanning electron microscopy (SEM) images indicate that the three electrodes have a similar morphology and porosity, so the doped carbon has no noticeable impact on the electrode morphology. In addition, EDS mapping of Pt, O, and F elements confirms a uniform distribution of the elements in the electrodes, as presented in Figures S2 and S3, so a homogeneous microenvironment around the Pt catalyst particles has been created in each electrode to investigate the effect of microenvironment.

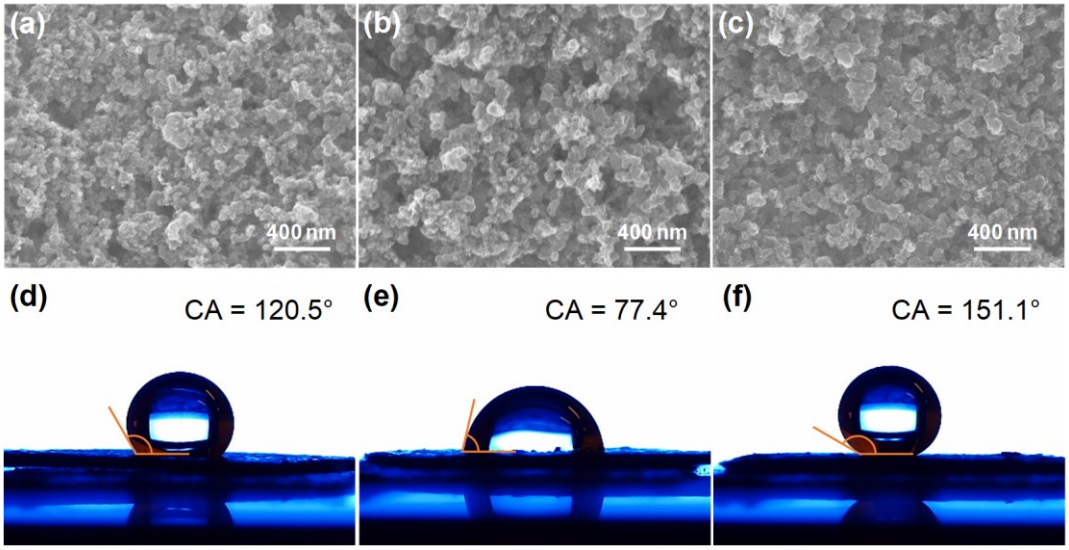

Figure 2. Characterization of the electrodes. (a–c) Representative SEM images of the (a) Pt/C, (b) Pt/C-O-12, and (c) Pt/C-F-800 electrodes. (d–f) Contact angles measured on the three electrodes with deionized water: (d) Pt/C, (e) Pt/C-O-12, and (f) Pt/C-F-800 electrodes.

In the prepared electrodes, the major impact of the doping is on the wetting properties of the carbon support: O-doping makes it more hydrophilic, while F-doping increases the hydrophobicity. To quantify their wetting properties, contact angles were measured on the as-prepared electrodes (after mixing with Pt nanoparticles and Nafion solution and deposition on a substrate). As shown in Figure 2d–f, the Pt/C electrode exhibits a contact angle of 120.5° (Figure 2d), and the Pt/C-O-12 electrode is more hydrophilic with a smaller contact angle of 77.4° and (Figure 2e), while the Pt/C-F-800 electrode is more hydrophobic with a larger contact angle of 151.1° (Figure 2f), showing the different wetting properties of the electrodes. As the same amount of Nafion was used in each electrode, the large difference in their contact angles indicates that their wetting properties are mainly determined by the carbon support itself, with a weak influence from the Nafion. Thus, we prepared a series of electrodes with the same Pt nanocatalyst and morphology but different

microenvironments over a wide range of hydrophilicity and hydrophobicity to investigate the effect on the electrocatalysis.

The electro-oxidation of aqueous N_2H_4 to gaseous N_2 on Pt catalyst was selected as a model reaction to study the effect of microenvironment in gas-evolving electrocatalysis. The prepared electrodes were tested for N_2H_4 electro-oxidation in a gas-tight two-compartment electrochemical cell (H-cell) with an electrolyte containing 0.5 M phosphate buffer solution (PBS) and 0.1 M N_2H_4, as illustrated in Figure S4. In particular, the neutral PBS electrolyte was used to minimize the non-Faradaic dehydrogenation process.[39] All potentials were iR-compensated using the positive-feedback mode and converted to the reversible hydrogen electrode (RHE) scale in this work. Linear sweep voltammetry (LSV) was first conducted to evaluate the electrocatalytic performance. As shown in Figure 3a, the Pt/C, Pt/C-O-12, and Pt/C-F-800 electrodes showed a similar onset potential of around 0.15 V vs RHE, but both the Pt/C-O-12 and Pt/C-F-800 electrodes showed higher current densities than the Pt/C, with the Pt/C-O-12 having the highest current density among the three. The fluctuations of current in the curves were caused by the formation and detachment of gas bubbles,[19,40] as will be discussed later. To exclude the possible contribution of activity from the carbon support, electrodes with carbon black only (no Pt catalyst) were tested as a background. As shown in Figure 3a, the carbon supports all showed a negligible current density at potentials <0.6 V vs RHE. Therefore, the different current densities in the LSV curves indicated a major effect of the microenvironment on the reaction rate.

Bulk electrolysis was further performed to measure the electrocatalytic activity at potentials ranging from 0.3 to 0.6 V vs RHE, as shown in Figure 3b. The current densities in the bulk electrolysis are lower than those in the corresponding LSV curves for each electrode, due to the difference between the two measurement methods. The current density increased rapidly with the overpotential, but the increase was slower than the exponential trend, likely due to the faster generation of gas bubbles that affected the activity at higher overpotentials. The Pt/C-F-800 electrode showed a current density of ~19.4 mA cm^{-2} at 0.5 V vs RHE, which is ~46% higher than that on the Pt/C electrode (~13.3 mA cm^{-2}). The Pt/C-O-12 electrode achieved an even higher current density of ~29.6 mA cm^{-2} at the potential, which is around 123% higher than that on the Pt/C electrode. Therefore, the bulk electrolysis data showed the same order of activities as that revealed by the LSV measurements, confirming that both the O-doped and F-doped carbon support enhanced the electrocatalytic performance for N_2H_4 electro-oxidation, despite the same Pt catalyst loading and similar electrode morphology.

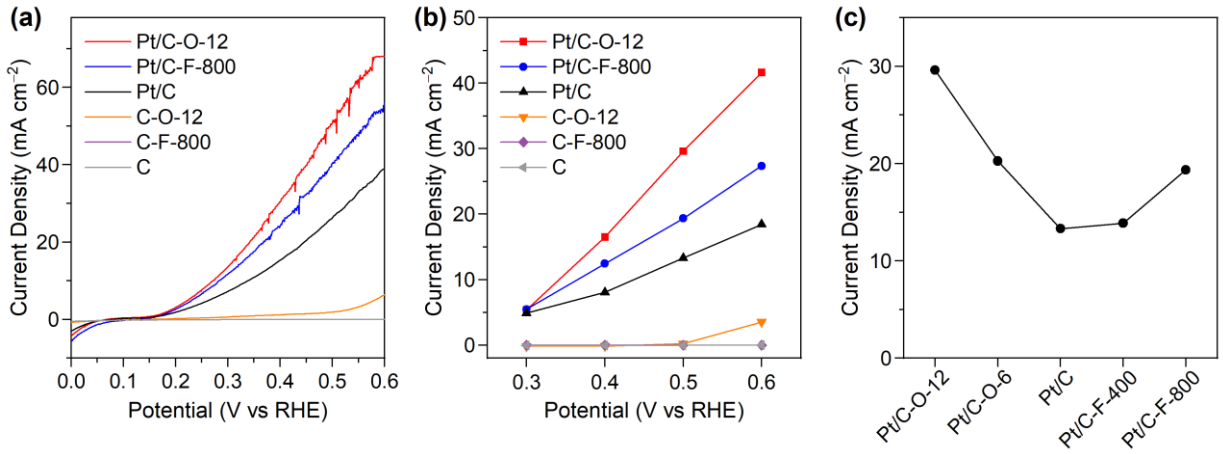

Figure 3. Comparison of the electrocatalytic performance of different electrodes in Ar-saturated 0.5 M PBS + 0.1 M N_2H_4 electrolyte. (a) LSV curves measured on different electrodes (with and without Pt catalyst). The fluctuations of current were caused by the formation and detachment of gas bubbles. Scan rate = 10 mV s^{-1}. (b) Current densities of bulk electrolysis measured on different electrodes at selected potentials. (c) Comparison of bulk electrolysis current densities measured at 0.5 V vs RHE on the electrodes with different O- or F-doping levels.

To further examine the effect of the O- or F-doping level, we prepared two more electrodes, Pt/C-O-6 and Pt/C-F-400, of which the former contains O-doped carbon black prepared with 6-h acidification treatment and the latter has F-doped carbon black prepared with an initial PTFE mass of 400 mg. TEM images and XPS spectra of the doped carbon black as well as SEM images of the corresponding electrodes are presented in Figure S5, which indicate a similar morphology of the electrodes but different levels of doping. Then we tested and compared the five electrodes for the N_2H_4 electro-oxidation reaction at 0.5 V vs RHE, as shown in Figure 3c. Compared to the Pt/C electrode with a current density of 13.3 mA cm^{-2}, the current density increased to 20.2 and 29.6 mA cm^{-2} on the Pt/C-O-6 and Pt/C-O-12 electrodes, respectively. The current density on the F-doped electrodes was also positively correlated with the F-doping level, which increased slightly to 13.9 mA cm^{-2} on the Pt/C-F-400 electrode and further increased to 19.4 mA cm^{-2} on Pt/C-F-800. The data confirmed that both O-doped and F-doped carbon support in the microenvironment enhanced the electrocatalytic activity of the Pt catalyst for N_2H_4 electro-oxidation.

As the electrodes have the same Pt catalyst and a similar morphology, the difference in their electrocatalytic performance should be attributed to the carbon supports with distinct wetting properties. Figure 4a summarizes the contact angles measured on the five electrodes. The contact angles of the as-prepared Pt/C-O-6 and Pt/C-O-12 electrodes are 72.4° and 72.3°, respectively, which are smaller than that of the Pt/C electrode (120.5°) and confirm the increased hydrophilicity. In contrast, the F-doped carbon makes the electrodes more hydrophobic, with larger contact angles of 151.1° and 154.7° for the Pt/C-F-400 and Pt/C-F-800 electrodes, respectively. However, these

contact angles were measured on the as-prepared electrodes, while their wetting states most likely evolve during electrochemical tests due to the interaction with electrolyte under applied potentials, as evidenced by the time-dependent measurement in Figure S6. Therefore, we further measured their contact angles after being tested for the N_2H_4 electro-oxidation at 0.5 V vs RHE for 30 min, which should reflect their stabilized wetting states. As exhibited in Figure 4a, the contact angles decreased to various degrees after the test. The contact angle of the Pt/C electrode dropped from 120.5° to 74.0°. The Pt/C-O-6 and Pt/C-O-12 electrodes showed similar contact angles initially, while their post-reaction contact angles were found to be 32.4° and 19.7°, respectively, indicating that a higher O-doping level made the electrode more hydrophilic. The post-reaction contact angles for the Pt/C-F-400 and Pt/C-F-800 electrodes were measured to be 125.7° and 143.6°, respectively, indicating that the carbon support with a higher F-doping level was more effective in maintaining the electrode hydrophobicity.

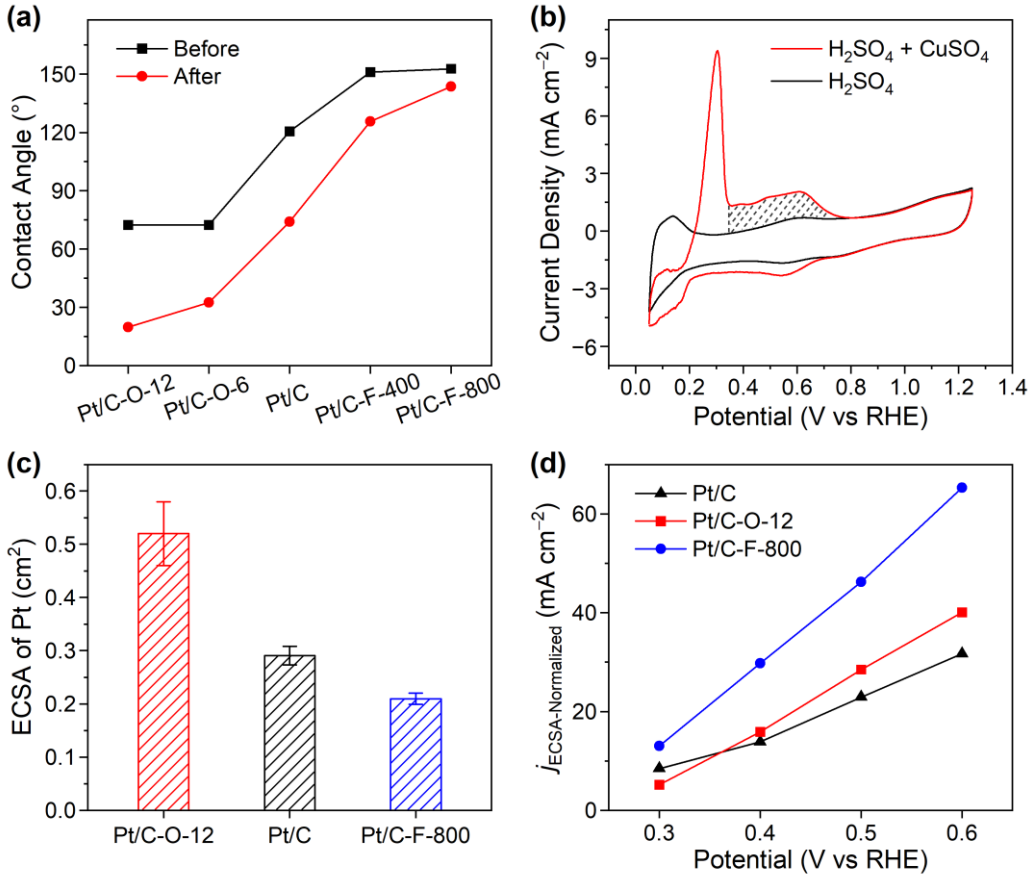

Figure 4. Effect of electrode wetting properties on the ECSA and exposure of Pt catalyst to the electrolyte. (a) Contact angles measured on the electrodes before and after N_2H_4 electro-oxidation reaction at 0.5 V vs RHE for 30 min. (b) CV scans recorded on the Pt/C-O-12 electrode in 0.5 M H_2SO_4 electrolyte (black line) and in 0.5 M H_2SO_4 + 5 mM $CuSO_4$ electrolyte (red line), respectively. The slashed peak area corresponds to the charges associated with the stripping of

underpotential deposited Cu. Scan rate = 10 mV s^{-1}. (c) The ECSA of Pt catalyst in the electrodes determined using the Cu UPD method. (d) ECSA-normalized current densities of bulk electrolysis measured on the different electrodes.

The wetting state of an electrode determines how much of the catalyst surface area is wetted by the electrolyte and thus available for aqueous N_2H_4 to adsorb and react. Compared to the Pt/C electrode, the Pt/C-O-12 electrode is more hydrophilic with more Pt surface sites wetted by the electrolyte. In contrast, the Pt/C-F-800 electrode is more hydrophobic and favors gas, so it should be less wetted by the electrolyte. To confirm this, we measured the electrochemically active surface area (ECSA) of Pt catalyst in the electrodes using Cu underpotential deposition (UPD) method,[41] in which a monolayer of Cu is deposited on Pt surface (but not on the carbon support) at potentials more positive than that required for bulk deposition. As shown in Figure 4b, cyclic voltammetry (CV) scans were first recorded on the electrode in 0.5 M H_2SO_4 electrolyte, and then in 0.5 M H_2SO_4 + 5 mM $CuSO_4$ electrolyte, where the features for the deposition and stripping of Cu can be identified. The slashed peak area in Figure 4b corresponds to the charges associated with the stripping of underpotential deposited Cu, which was converted to the ECSA of Pt using a conversion factor of 420 μC cm^{-2}.[41] As a result, the ECSA of Pt catalyst was determined to be 0.29 ± 0.02 cm^2 in the Pt/C electrode, which increased to 0.52 ± 0.06 cm^2 in the Pt/C-O-12 electrode, but decreased slightly to 0.21 ± 0.01 cm^2 in the Pt/C-F-800 electrode, as plotted in Figure 4c. The ECSA of Pt in the Pt/C-O-12 electrode is around 80% higher than that in the Pt/C electrodes, thus allowing more Pt surface sites to contact the electrolyte and catalyze the electro-oxidation of N_2H_4, which should mainly account for the enhanced performance. Nevertheless, the lower ECSA of Pt in the Pt/C-F-800 electrode cannot explain its higher reaction rate than the Pt/C electrode. This is counterintuitive and implies that the electrocatalytic performance is also affected by other factors, particularly the in situ generated gas bubbles.

In the N_2H_4 electro-oxidation reaction, the formation and detachment of N_2 gas bubbles will change the contact area of the Pt catalyst with the electrolyte, thus impacting the reaction kinetics, such as the fluctuation of current in the LSV curves in Figure 3a. Typically, there are four stages for gas bubble dynamics on a gas-evolving electrode, including nucleation, growth, coalescence, and detachment.[17,18] Along with the nucleation and growth of N_2 gas bubbles on the Pt catalyst, more and more Pt surface sites are covered by the bubbles and are thus blocked from the electrolyte. When the bubbles reach a critical size at which the buoyant force is strong enough to counter the adhesion force, the bubbles detach from the electrode, and then the Pt surface sites become active again to catalyze the N_2H_4 electro-oxidation. This process will cause a “dip” in the current curve, such as those in Figure 3a. Therefore, the electrocatalytic performance is also impacted by the gas bubble dynamics, which depend on the adhesion and wetting properties of the electrodes.[22–24] To compare how efficiently the wetted Pt active sites are catalyzing the reaction during the gas bubble

generation/detachment cycles, we normalized the bulk electrolysis current densities by the ECSA of Pt catalyst in each electrode, as shown in Figure 4d. Interestingly, the ECSA-normalized activity of the Pt/C-F-800 electrode is almost double that of the Pt/C electrode, confirming the enhanced activity per Pt active site in the Pt/C-F-800 electrode due to the hydrophobic microenvironment and the resulting gas bubble dynamics.

To investigate the gas bubble dynamics on different electrodes, chronopotentiometric curves were first recorded on them at a current density of 10 mA cm^{-2}, so that the same amount of N_2 gas was generated per unit time on each electrode for a meaningful comparison. As shown in Figure 5a, the curves exhibit detailed features of the fluctuations of potential, which were caused by the generation and detachment of gas bubbles.[17,42,43] The overpotential fluctuations in the curves are nearly periodic, and the average periods are determined to be 0.77 ± 0.02, 0.63 ± 0.03, and 0.45 ± 0.02 s for the Pt/C-O-12, Pt/C, and Pt/C-F-800 electrodes, respectively, as presented in Figure 5b. According to the fluctuation periods, the Pt/C-F-800 electrode leads to the shortest cycle or lifetime of the gas bubble dynamics,[22,23] which facilitates the timely release of gas bubbles. To reveal how the hydrophobic microenvironment causes faster removal of gas bubbles, we observed the dynamic evolutions of gas bubbles on the Pt/C and Pt/C-F-800 electrodes using optical microscopy, with two videos recorded under chronopotentiometric conditions (current density = 10 mA cm^{-2}), which are presented as Supporting Videos S1 and S2, respectively. A major difference we observed is that the gas bubbles on the Pt/C-F-800 electrode were much more mobile and diffused quickly on the electrode surface to coalesce and form larger bubbles. To illustrate this, an image sequence was extracted from Video S2 at selected times to demonstrate the fast diffusion and growth of gas bubbles on the Pt/C-F-800 electrode, as shown in Figure 5c−h. This accelerated the growth of the gas bubbles to reach the critical size, and facilitated faster detachment and release of gas bubbles from Pt catalyst, thus recovering the active sites to enhance the electrocatalytic performance.

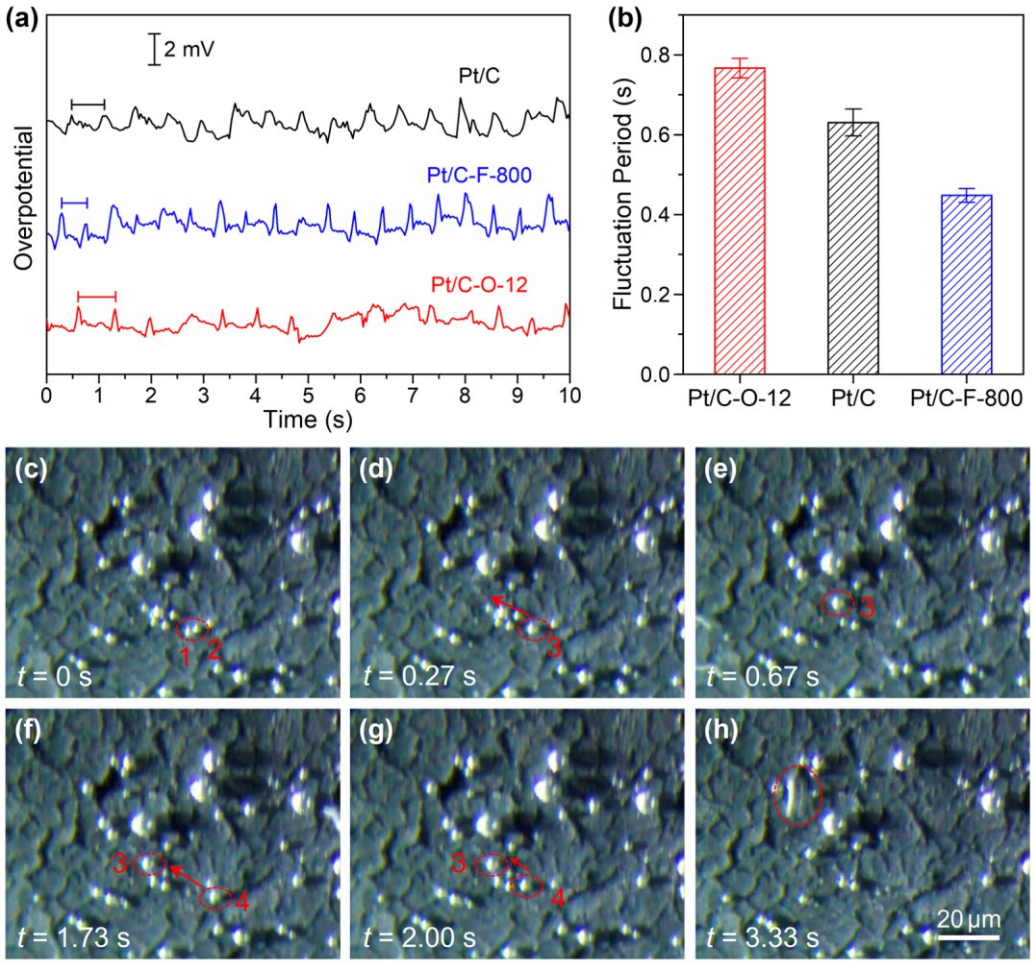

Figure 5. Gas bubble formation and detachment. (a) Chronopotentiometric curves recorded on the electrodes for N_2H_4 electro-oxidation at a current density of 10 mA cm^{-2}. (b) Average periods for the fluctuations of potential in (a). (c–h) Image sequence, extracted from the optical microscopy video clip (Video S2 in the Supporting Information), showing the fast diffusion and growth of gas bubbles on the Pt/C-F-800 electrode: (c–d) bubble 1 and 2 merged into bubble 3; (d–e) bubble 3 moved on the surface and absorbed bubbles along the pathway; (e–f) bubble 4 was formed; (f–g) bubble 4 moved on the surface; (g–h) bubble 4 further moved and merged with bubble 3, and then detached from the surface.

In addition to the lifetime of the gas bubbles, the bubble dynamics are also determined by the critical bubble size at detachment. As a hydrophobic surface favors gas, the adhesion force of gas bubbles on the Pt/C-F-800 electrode should be larger than that on the Pt/C electrode (see the estimations in Note 1 of the Supporting Information),[30] leading to a larger critical bubble size as a larger buoyant force is needed to counter the adhesion force. Indeed, as exhibited in Figure S7, side-view optical microscopy images of the electrode-electrolyte interfaces showed larger gas bubbles on the Pt/C-F-800 electrode than that on the Pt/C electrode. To quantify this, we analyzed

the Supporting Videos S1 and S2 and measured the diameters of the gas bubbles at detachment. Thus, we obtained the statistics of the critical bubble diameters, which are 6.75 ± 1.75 and 7.65 ± 2.15 μm for the Pt/C and Pt/C-F-800 electrodes, respectively, as presented in Figure S8. The larger critical bubble size on the hydrophobic Pt/C-F-800 electrode agrees with previous studies and our analysis above.[30]

By combining the two factors (average lifetime and critical bubble size) together, we can now quantitatively compare the gas bubble dynamics on the electrodes. For the above measurements under chronopotentiometric conditions, we can estimate the gas bubble growth rates on the two electrodes, which are 256.6 and 522.7 $\mu m^3 s^{-1}$ on the Pt/C and Pt/C-F-800 electrodes, respectively, as derived in the Note 2 of the Supporting Information. Despite the larger critical size of bubbles on the Pt/C-F-800 electrode, it takes shorter time for the bubbles to reach the critical size, so that the gas bubble growth rate on the Pt/C-F-800 electrode is around double that on the Pt/C electrode. This benefits from the fast diffusion and coalescence of gas bubbles on the Pt/C-F-800 electrode, as evidenced by the optical microscopy videos (Video S1 and S2) and images (Figure 5c–h), which accelerate the detachment of the generated gas bubbles and thus the recovery of the Pt active sites. Therefore, the shorter lifetime of the gas bubbles compensates the minor disadvantage of the lower ECSA and larger critical bubble size on the Pt/C-F-800 electrode, so that the overall effect of gas bubble dynamics is still more favorable for a higher reaction rate on the Pt/C-F-800 electrode than on the Pt/C electrode. Looking back at the data in Figure 4d, the higher ECSA-normalized activity on the Pt/C-F-800 electrode also confirms that each Pt active site in the electrode is more effective in catalyzing the reaction than the Pt/C electrode, benefiting from the faster gas bubble release and catalytic site recovery.[22,23]

Compared to previous works mainly focused on superaerophobic/superhydrophilic electrodes by utilizing the nanostructured morphology,[25–32] we designed a series of electrodes with the same catalyst and morphology but with different wetting properties of the microenvironment over a wide range of hydrophilicity and hydrophobicity, enabling a meaningful comparison and elucidation of the effect of the microenvironment. The large tunability of the wetting condition, from hydrophilic to hydrophobic, by doping of the carbon support, ensures that this approach can span most of the design conditions for practical applications.[24] Furthermore, we discovered that the hydrophilic and hydrophobic microenvironments dominate different factors in the electrocatalytic process — the exposure of catalytic sites to the electrolyte and the removal of generated gas bubbles, respectively; both are essential for efficient electrocatalysis. Compared to the nanowire-based electrodes or the template-patterned method,[44,45] our strategy of tuning the microenvironment using doped carbon as the catalyst support can be a facile, generally applicable, and scalable method to improve gas-evolving electrocatalysis. Our work provides new insights and guidance for the rational design of efficient electrodes and devices for renewable energy conversions.

In summary, we have demonstrated that the N_2H_4 electro-oxidation reaction, as an example of gas-evolving reaction, is very sensitive to the wetting properties of catalyst microenvironment. For carbon-supported Pt catalyst, both O-doped and F-doped carbon black were used as the catalyst support to tune the microenvironment over a wide range of wetting conditions. As a result, the more hydrophilic electrode with O-doped carbon showed a 123% higher activity than the electrode with pristine carbon, benefiting from the enhanced wetting and exposure of the Pt catalytic sites to the electrolyte. Although the electrode with F-doped carbon is more hydrophobic with a lower exposure of Pt catalytic sites to N_2H_4, it still exhibited a 46% higher activity than that with pristine carbon. This was attributed to the accelerated surface diffusion, coalescence, and detachment of the generated N_2 gas bubbles, which would otherwise block the Pt active sites from catalyzing the reaction. Therefore, the mass transport of both liquid and gaseous species, which is highly sensitive to the wetting state of the microenvironment, plays a critical role in determining the electrocatalytic performance. Our work also suggests that tuning the microenvironment using doped carbon as the catalyst support can be a generally applicable method to improve gas-evolving electrocatalysis.

ASSOCIATED CONTENT

Supporting Information

The Supporting Information is available free of charge at …

Experimental methods, additional materials characterization and electrochemical measurements (Figures S1−S8) (PDF)

Videos S1 (MPG) and S2 (MPG)

AUTHOR INFORMATION

ORCID: Kaige Shi: 0000-0003-1372-0210
Zackary S. Parsons: 0000-0001-7945-5128
Xiaofeng Feng: 0000-0002-9473-2848

Notes: The authors declare no competing financial interest.

ACKNOWLEDGMENTS

This material is based upon work supported by the National Science Foundation (NSF) under Grant No. 1943732. The authors acknowledge the use of an XPS instrument supported by the NSF MRI: ECCS: 1726636.

REFERENCES

(1) Stamenkovic, V. R.; Strmcnik, D.; Lopes, P. P.; Markovic, N. M. Energy and fuels from electrochemical interfaces. *Nat. Mater.* **2017**, *16*, 57−69.

(2) Wang, X. X.; Swihart, M. T.; Wu, G. Achievements, challenges and perspectives on cathode catalysts in proton exchange membrane fuel cells for transportation. *Nat. Catal.* **2019**, *2*, 578−589.

(3) De Luna, P.; Hahn, C.; Higgins, D.; Jaffer, S. A.; Jaramillo, T. F.; Sargent, E. H. What would it take for renewably powered electrosynthesis to displace petrochemical processes? *Science* **2019**, *364*, eaav3506.

(4) Yu, Z. Y.; Duan, Y.; Feng, X. Y.; Yu, X.; Gao, M. R.; Yu, S. H. Clean and affordable hydrogen fuel from alkaline water splitting: past, recent progress, and future prospects. *Adv. Mater.* **2021**, *33*, 2007100.

(5) Linnemann, J.; Kanokkanchana, K.; Tschulik, K. Design strategies for electrocatalysts from an electrochemist's perspective. *ACS Catal.* **2021**, *11*, 5318−5346.

(6) Xing, Z.; Hu, L,; Ripatti, D. S.; Hu, X.; Feng, X. Enhancing carbon dioxide gas-diffusion electrolysis by creating a hydrophobic catalyst microenvironment. *Nat. Commun.* **2021**, *12*, 136.

(7) Yang, K.; Kas, R.; Smith, W. A.; Burdyny, T. Role of the carbon-based gas diffusion layer on flooding in a gas diffusion electrode cell for electrochemical CO_2 reduction. *ACS Energy Lett.* **2021**, *6*, 33−40.

(8) Xing, Z.; Hu, X.; Feng, X. Tuning the microenvironment in gas-diffusion electrodes enables high-rate CO2 electrolysis to formate. *ACS Energy Lett.* **2021**, *6*, 1694−1702.

(9) Liu, G.; Wong, W. S.; Kraft, M.; Ager, J. W.; Vollmer, D.; Xu, R. Wetting-regulated gas-involving (photo)electrocatalysis: biomimetics in energy conversion. *Chem. Soc. Rev.* **2021**, *50*, 10674−10699.

(10) Xing, Z.; Shi, K.; Parsons, Z. S.; Feng, X. Interplay of active sites and microenvironment in high-rate electrosynthesis of H_2O_2 on doped carbon. *ACS Catal.* **2023**, *13*, 2780−2789.

(11) Law, K. Y. Definitions for hydrophilicity, hydrophobicity, and superhydrophobicity: getting the basics right. *J. Phys. Chem. Lett.* **2014**, *5*, 686−688.

(12) Nesbitt, N. T.; Burdyny, T.; Simonson, H.; Salvatore, D.; Bohra, D.; Kas, R.; Smith, W. A. Liquid–solid boundaries dominate activity of CO_2 reduction on gas-diffusion electrodes. *ACS Catal.* **2020**, *10*, 14093−14106.

(13) Wang, Y.; Zou, Y.; Tao, L.; Wang, Y.; Huang, G.; Du, S.; Wang, S. Rational design of three-phase interfaces for electrocatalysis. *Nano Res.* **2019**, *12*, 2055−2066.

(14) Sides, P. J. Phenomena and Effects of Electrolytic Gas Evolution. *Modern Aspects of Electrochemistry*; Springer, 1986; pp 303−354.

(15) Kashchiev, D. *Nucleation: Basic Theory and Applications*; Butterworth-Heinemann: Oxford, U.K., 2000.
(16) Zeng, K.; Zhang, D. Recent progress in alkaline water electrolysis for hydrogen production and applications. *Prog. Energy Combust. Sci.* **2010**, *36*, 307−326.
(17) Fernandez, D.; Maurer, P.; Martine, M.; Coey, J. M. D.; Möbius, M. E. Bubble formation at a gas-evolving microelectrode. *Langmuir* **2014**, *30*, 13065−13074.
(18) Zhao, X.; Ren, H.; Luo, L. Gas bubbles in electrochemical gas evolution reactions. *Langmuir* **2019**, *35*, 5392−5408.
(19) Lake, J. R.; Soto, A. M.; Varanasi, K. K. Impact of bubbles on electrochemically active surface area of microtextured gas-evolving electrodes. *Langmuir* **2022**, *38*, 3276−3283.
(20) Chen, Q.; Luo, L. Correlation between gas bubble formation and hydrogen evolution reaction kinetics at nanoelectrodes. *Langmuir* **2018**, *34*, 4554−4559.
(21) Angulo, A.; van der Linde, P.; Gardeniers, H.; Modestino, M.; Rivas, D. F. Influence of bubbles on the energy conversion efficiency of electrochemical reactors. *Joule* **2020**, *4*, 555−579.
(22) Ho, C. N.; Hwang, B. J. Effect of hydrophobicity on the hydrophobic-modified polytetrafluoroethylene/PbO_2 electrode towards oxygen evolution. *J. Electroanal. Chem.* **1994**, *377*, 177−190.
(23) Meng, C.; Wang, B.; Gao, Z.; Liu, Z.; Zhang, Q.; Zhai, J. Insight into the role of surface wettability in electrocatalytic hydrogen evolution reactions using light-sensitive nanotubular TiO_2 supported Pt electrodes. *Sci. Rep.* **2017**, *7*, 41825.
(24) Iwata, R.; Zhang, L.; Wilke, K. L.; Gong, S.; He, M.; Gallant, B. M.; Wang, E. N. Bubble growth and departure modes on wettable/non-wettable porous foams in alkaline water splitting. *Joule* **2021**, *5*, 887−900.
(25) Lu, Z.; Sun, M.; Xu, T.; Li, Y.; Xu, W.; Chang, Z.; Ding, Y.; Sun, X.; Jiang, L. Superaerophobic electrodes for direct hydrazine fuel cells. *Adv. Mater.* **2015**, *27*, 2361−2366.
(26) Lu, Z.; Li, Y.; Lei, X.; Liu, J.; Sun, X. Nanoarray based "superaerophobic" surfaces for gas evolution reaction electrodes. *Mater. Horiz.* **2015**, *2*, 294−298.
(27) Feng, G.; Kuang, Y.; Li, Y.; Sun, X. Three-dimensional porous superaerophobic nickel nanoflower electrodes for high-performance hydrazine oxidation. *Nano Res.* **2015**, *8*, 3365−3371.
(28) Burdyny, T.; Graham, P. J.; Pang, Y.; Dinh, C. T.; Liu, M.; Sargent, E. H.; Sinton, D. Nanomorphology-enhanced gas-evolution intensifies CO_2 reduction electrochemistry. *ACS Sustainable Chem. Eng.* **2017**, *5*, 4031−4040.
(29) Xu, W.; Lu, Z.; Sun, X.; Jiang, L.; Duan, X. Superwetting electrodes for gas-involving electrocatalysis. *Acc. Chem. Res.* **2018**, *51*, 1590−1598.

(30) Li, H.; Chen, S.; Zhang, Y.; Zhang, Q.; Jia, X.; Zhang, Q.; Gu, L.; Sun, X.; Song, L.; Wang, X. Systematic design of superaerophobic nanotube-array electrode comprised of transition-metal sulfides for overall water splitting. *Nat. Commun.* **2018**, *9*, 2452.
(31) Yu, X.; Yu, Z. Y.; Zhang, X. L.; Zheng, Y. R.; Duan, Y.; Gao, Q.; Wu, R.; Sun, B.; Gao, M. R.; Wang, G.; et al. "Superaerophobic" nickel phosphide nanoarray catalyst for efficient hydrogen evolution at ultrahigh current densities. *J. Am. Chem. Soc.* **2019**, *141*, 7537−7543.
(32) Andaveh, R.; Darband, G. B.; Maleki, M.; Rouhaghdam, A. S. Superaerophobic/superhydrophilic surfaces as advanced electrocatalysts for the hydrogen evolution reaction: a comprehensive review. *J. Mater. Chem. A* **2022**, *10*, 5147−5173.
(33) Trogadas, P.; Fuller, T. F.; Strasser, P. Carbon as catalyst and support for electrochemical energy conversion. *Carbon* **2014**, *75*, 5−42.
(34) Wang, G.; Sun, G.; Wang, Q.; Wang, S.; Sun, H.; Xin, Q. Effect of carbon black additive in Pt black cathode catalyst layer on direct methanol fuel cell performance. *Int. J. Hydrog. Energy* **2010**, *35*, 11245−11253.
(35) Wu, G.; Li, D.; Dai, C.; Wang, D.; Li, N. Well-dispersed high-loading Pt nanoparticles supported by shell−core nanostructured carbon for methanol electrooxidation. *Langmuir* **2008**, *24*, 3566−3575.
(36) Wu, G.; Swaidan, R.; Li, D.; Li, N. Enhanced methanol electro-oxidation activity of PtRu catalysts supported on heteroatom-doped carbon. *Electrochim. Acta* **2008**, *53*, 7622−7629.
(37) Lu, Z.; Chen, G.; Siahrostami, S.; Chen, Z.; Liu, K.; Xie, J.; Liao, L.; Wu, T.; Lin, D.; Liu, Y.; et al. High-efficiency oxygen reduction to hydrogen peroxide catalysed by oxidized carbon materials. *Nat. Catal.* **2018**, *1*, 156−162.
(38) Biffinger, J. C.; Kim, H. W.; DiMagno, S. G. The polar hydrophobicity of fluorinated compounds. *ChemBioChem* **2004**, *5*, 622−627.
(39) Wang, J.; Khaniya, A.; Hu, L.; Beazley, M. J.; Kaden, W. E.; Feng, X. A bifunctional catalyst for efficient dehydrogenation and electro-oxidation of hydrazine. *J. Mater. Chem. A* **2018**, *6*, 18050−18056.
(40) Kwan, J. T. H.; Nouri-Khorasani, A.; Bonakdarpour, A.; McClement, D. G.; Afonso, G.; Wilkinson, D. P. Frequency analysis of water electrolysis current fluctuations in a PEM flow cell: Insights into bubble nucleation and detachment. *J. Electrochem. Soc.* **2022**, *169*, 054531.
(41) Green, C. L.; Kucernak, A. Determination of the platinum and ruthenium surface areas in platinum−ruthenium alloy electrocatalysts by underpotential deposition of copper. I. Unsupported catalysts. *J. Phys. Chem. B* **2002**, *106*, 1036−1047.
(42) Gabrielli, C.; Huet, F.; Nogueira, R. P. Fluctuations of concentration overpotential generated at gas-evolving electrodes. *Electrochim. Acta* **2005**, *50*, 3726−3736.

(43) Kwan, J. T. H.; Nouri-Khorasani, A.; Bonakdarpour, A.; McClement, D. G.; Afonso, G.; Wilkinson, D. P. Frequency analysis of water electrolysis current fluctuations in a PEM flow cell: Insights into bubble nucleation and detachment. *J. Electrochem. Soc.* **2022**, *169*, 054531.
(44) Song, Q.; Xue, Z.; Liu, C.; Qiao, X.; Liu, L.; Huang, C.; Liu, K.; Li, X.; Lu, Z.; Wang, T. General strategy to optimize gas evolution reaction via assembled striped-pattern superlattices. *J. Am. Chem. Soc.* **2020**, *142*, 1857−1863.
(45) Zhang, C.; Xu, Z.; Han, N.; Tian, Y.; Kallio, T.; Yu, C.; Jiang, L. Superaerophilic/superaerophobic cooperative electrode for efficient hydrogen evolution reaction via enhanced mass transfer. *Sci. Adv.* **2023**, *9*, eadd6978.

Table of Contents (TOC) Graphic: